Unveiling the Catalytic Potential of Topological Nodal-Line Semimetal AuSn4 for Hydrogen Evolution and CO2 Reduction

Article *in* The Journal of Physical Chemistry Letters · March 2023

DOI: 10.1021/acs.jpclett.3c00113

CITATIONS
3

READS
126

12 authors, including:

D. W. Boukhvalov
Nanjing Forestry University
291 PUBLICATIONS **14,995** CITATIONS
SEE PROFILE

Gianluca D'Olimpio
Università degli Studi dell'Aquila
42 PUBLICATIONS **602** CITATIONS
SEE PROFILE

Federico Mazzola
University of St Andrews
110 PUBLICATIONS **2,343** CITATIONS
SEE PROFILE

Chia Nung Kuo
National Cheng Kung University, Tainan
137 PUBLICATIONS **1,573** CITATIONS
SEE PROFILE

THE JOURNAL OF PHYSICAL CHEMISTRY LETTERS
A JOURNAL OF THE AMERICAN CHEMICAL SOCIETY

pubs.acs.org/JPCL

Letter

Unveiling the Catalytic Potential of Topological Nodal-Line Semimetal $AuSn_4$ for Hydrogen Evolution and CO_2 Reduction

Danil W. Boukhvalov,[#] Gianluca D'Olimpio,[#] Federico Mazzola, Chia-Nung Kuo, Sougata Mardanya, Jun Fujii, Grazia Giuseppina Politano, Chin Shan Lue, Amit Agarwal, Ivana Vobornik, Piero Torelli, and Antonio Politano*

Cite This: *J. Phys. Chem. Lett.* 2023, 14, 3069−3076

Read Online

ACCESS | Metrics & More | Article Recommendations | Supporting Information

ABSTRACT: In recent years, the correlation between the existence of topological electronic states in materials and their catalytic activity has gained increasing attention, due to the exceptional electron conductivity and charge carrier mobility exhibited by quantum materials. However, the physicochemical mechanisms ruling catalysis with quantum materials are not fully understood. Here, we investigate the chemical reactivity, ambient stability, and catalytic activity of the topological nodal-line semimetal $AuSn_4$. Our findings reveal that the surface of $AuSn_4$ is prone to oxidation, resulting in the formation of a nanometric SnO_2 skin. This surface oxidation significantly enhances the material's performance as a catalyst for the hydrogen evolution reaction in acidic environments. We demonstrate that the peculiar atomic structure of oxidized $AuSn_4$ enables the migration of hydrogen atoms through the Sn−O layer with a minimal energy barrier of only 0.19 eV. Furthermore, the Volmer step becomes exothermic in the presence of Sn vacancies or tin-oxide skin, as opposed to being hindered in the pristine sample, with energy values of −0.62 and −1.66 eV, respectively, compared to the +0.46 eV energy barrier in the pristine sample. Our model also suggests that oxidized $AuSn_4$ can serve as a catalyst for the hydrogen evolution reaction in alkali media. Additionally, we evaluate the material's suitability for the carbon dioxide reduction reaction, finding that the presence of topologically protected electronic states enhances the migration of hydrogen atoms adsorbed on the catalyst to carbon dioxide.

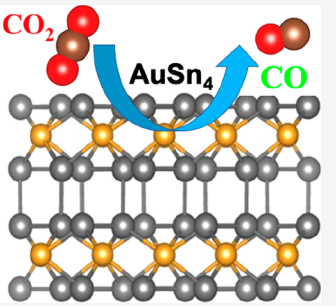

Quantum materials have attracted considerable attention in the past decade for the exotic phenomena enabled by their topologically nontrivial states.[1−5] While most existing investigations are still focused on fundamental physics, it is well recognized that the goal of this vast scientific community is to (i) identify and (ii) implement technological applications, possibly scalable at the industrial level, exploiting the quantum phenomena associated with the topological protection of their electronic states. In recent years, topological materials have been proposed for applications in various fields, such as energy,[6] optoelectronics,[7] electronics,[8] and recently topological catalysis.[9−11] Especially, catalysis with quantum materials represents a new promising route in electrochemistry, considering that topological surface states mediate the charge transfer between the substrate and the adsorbed chemical species. Furthermore, the high carrier mobility associated with massless Fermions in topologically protected surface states with linear dispersion is beneficial for fast electron transfer. Accordingly, topological materials, naturally exhibiting (i) high electrical conductivity, (ii) nontrivial topologically protected surface states, and (iii) ultrahigh mobility charge carriers,[9,12,13] represent promising candidates for the development next-generation catalysts. Similarly, PtGa,[14] PtAl,[14] TaP,[15] NbP,[15] TaAs,[15] and NbAs[15] have been proposed as catalysts for the hydrogen evolution reaction (HER).

Recently, $PtSn_4$,[16] $PdSn_4$,[17,18] and $AuSn_4$[19,20] have been reported to display an exotic structure of Dirac node arcs, which can be categorized in a new class of topological materials, namely, topological nodal-line semimetals. Especially, $AuSn_4$ deserves particular attention, owing to the discovery of superconductivity,[12,21] strictly correlated with the presence of Dirac-cone electrons in topological surface states.

In contrast to van der Waals layered materials, in $AuSn_4$ the break of the metallic interlayer bonds originates in the topological surface states. Its chemical instability can be attributed to the formation of these broken bonds.[22−24] Therefore, to assess the catalytic properties of topological materials, it is necessary to consider the surface oxidation and its relationship with the topologically nontrivial states. In this study, we aim to elucidate the correlation between catalysis and surface chemical reactivity in topological nodal-line semimetal $AuSn_4$.

Received: January 12, 2023
Accepted: March 16, 2023

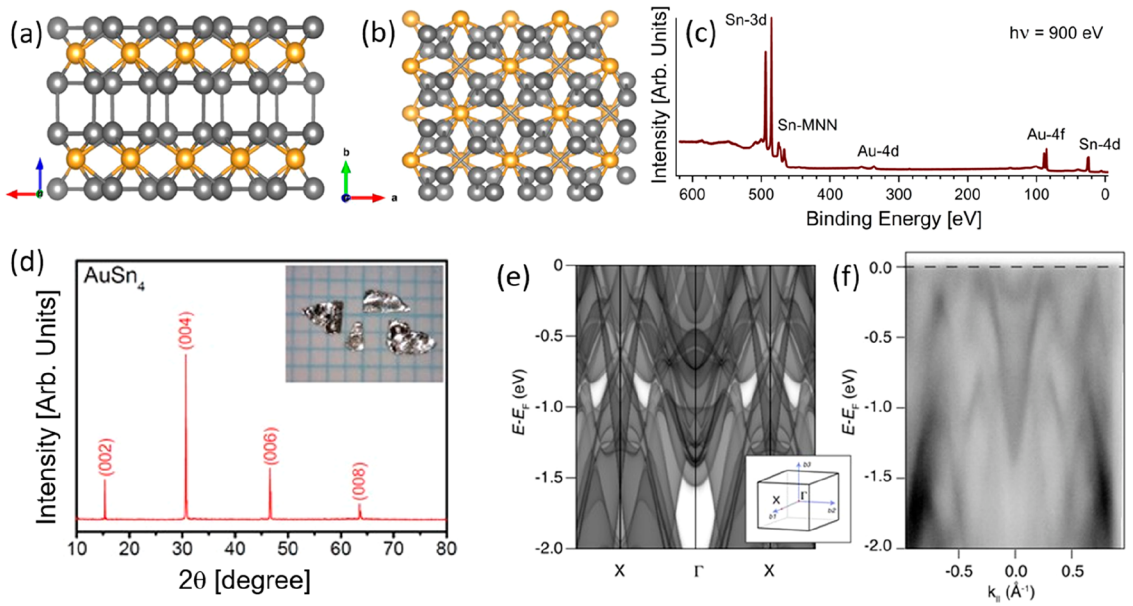

Figure 1. (a, b) Side and top views of the atomic structure of $AuSn_4$. Yellow and gray balls denote Au and Sn atoms, respectively. (c) XPS survey spectrum of as-cleaved $AuSn_4$. (d) XRD spectrum for a single crystal of $AuSn_4$. The inset shows a photograph of grown single crystals. (e) Bulk electronic structure of $AuSn_4$ obtained by density functional theory. Bands were obtained by projecting the available k_z within the whole Brillouin zone. (f) The corresponding ARPES data are shown as a sum of in-plane and out-of-plane light polarization, with photons of 48 eV. At this energy, it is possible to access the full Brillouin zone along Γ-X, along the orange line of the inset, and the photoemission matrix elements are favorable. The overall agreement between the calculated and the measured energy-momentum dispersion is evident.

Using surface-science spectroscopies and density functional theory (DFT), we demonstrate that the catalytic activity is driven by the self-assembled $SnO_2/AuSn_4$ heterostructure formed upon interaction of the $AuSn_4$ surface with ambient atmosphere. The diffusion of hydrogen atoms through the tin-oxide skin has a barrier of only 0.19 eV. Moreover, the Volmer step is energetically favorable in the presence surface oxidation (−1.66 eV), in contrast to the pristine surface. Moreover, both pristine and oxidized $AuSn_4$ surfaces represent suitable catalysts for the carbon dioxide reduction reaction, as the presence of topologically protected electronic states favor the migration of the hydrogen atom adsorbed on the catalyst toward carbon dioxide, with the following conversion of the noncovalently adsorbed CO_2 to −COOH or carboxyl groups.

$AuSn_4$ belongs to the space group *Aba*2 (No. 41), and its atomic structure has alternating Au and Sn layers with a Sn-terminated surface (Figure 1a,b). Despite the fact that O contamination is often observed in the bulk crystals of Sn-based alloys,[25] survey spectra obtained using X-ray photoelectron spectroscopy (XPS) (Figure 1c) reveal the absence of any such contamination in the bulk crystal. The crystal is oriented along a preferential (002) cleavage plane, as evidenced by the room-temperature X-ray diffraction (XRD) pattern (Figure 1d). The lattice constants evaluated from XRD are a = 6.497 ± 0.002 Å, b = 6.527 ± 0.002 Å, and c = 11.717 ± 0.002 Å, congruently with previous reports.[12] The single-crystal XRD pattern (Figure 1d) demonstrates that the basal plane of a cleaved crystal is perpendicular to the b-axis. Figure 1e shows the theoretical band structure along the high symmetry direction X-Γ-X (see the inset to Figure 1e for the Brillouin zone), with spectral weight projected for several k_z values. The theoretical band structure was experimentally validated by synchrotron-based angle-resolved photoelectron spectroscopy (ARPES, Figure 1f), which confirmed the occurrence of complex multibands system. Especially, the band structure (Figure 1e−f) shows a metallic character of the samples, with prominent intensity given by electron-like pockets located at the center of the Brillouin zone. These "pockets" correspond to the appearance of the peaks on the Fermi level in the density of states (DOS, Figure 2). One of

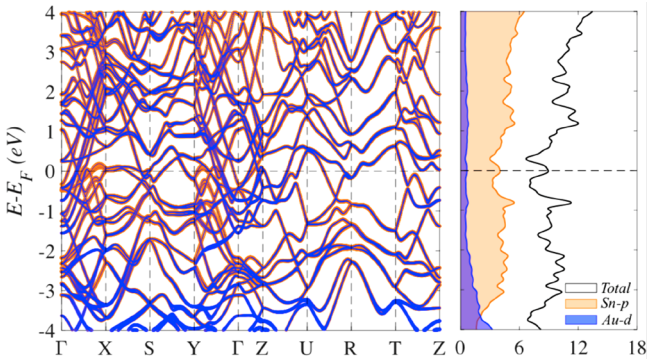

Figure 2. Orbital-resolved band structure (left) and total and partial densities of states of bulk $AuSn_4$ (right).

the peculiarities of topological materials, also observed in $AuSn_4$, is the absence of a clear separation between the orbitals of tin and gold in the valence band. Note that in contrast to topological materials with covalent bonds, in $AuSn_4$ gold and tin layers are held by metallic bonds, and therefore Au 5d and Sn 4d bands are overlapped (Figure 1).

To evaluate the chemical stability of the $AuSn_4$ surface, we modeled physisorption and further decomposition of ambient gases on $AuSn_4$. To account for defects naturally occurring in real samples, we modeled $AuSn_{3.88}$, by including one Sn vacancy in the surface layer of the supercell (Figure 3a). Note that the calculated formation energy of a single Sn vacancy on

https://doi.org/10.1021/acs.jpclett.3c00113
J. Phys. Chem. Lett. 2023, 14, 3069−3076

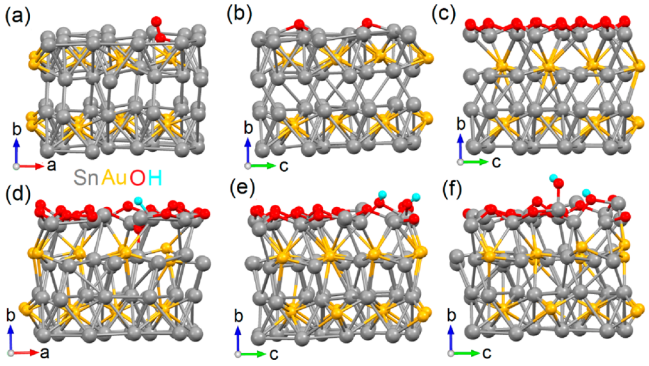

Figure 3. Optimized atomic structure of (a) molecular oxygen physisorbed on one Sn vacancy in the surface layer of $AuSn_{3.88}$, (b) oxygen molecule decomposed on the surface of $AuSn_4$, (c) formation of oxidized layer on the surface of $AuSn_4$. Panels d–f represent the various reactions steps of the HER on the oxidized surface of $AuSn_4$, namely (d) adsorption of hydrogen, (e) decomposition of water, and (f) first step of desorption of OH^- on the oxidized surface of $AuSn_4$.

the surface layer is 0.84 eV/Sn (81.2 kJ/mol). Thus, the amount of the vacancies in the surface layer is non-negligible.

In Table 1 the differential enthalpy and Gibbs free energy of physisorption at room temperature of carbon monoxide, water, and molecular oxygen are reported. Physisorption of carbon monoxide and water on a defect-free surface of $AuSn_4$ at room temperature is energetically unfavorable, as indicated by the positive value of the differential Gibbs free energy of physisorption (ΔG = +11.33 kJ/mol, ΔG = +30.3 kJ/mol, respectively). At room temperature, $AuSn_4$ is reactive only toward molecular oxygen (ΔG = −36.8 kJ/mol).

Table 1. Differential Enthalpy for Physisorption ΔH_{ads}, Differential Gibbs Free Energy at Room Temperature for Physisorption ΔG, and Differential Enthalpy of Decomposition ΔH_{dec} (all in kJ/mol) of Selected Molecules over the Defect-free Surface of $AuSn_4$ and the Defective Surface of $AuSn_{3.88}$

		physisorption		
substrate	molecule	ΔH_{ads} [kJ/mol]	ΔG [kJ/mol]	decomposition ΔH_{dec} [kJ/mol]
$AuSn_4$	CO	−8.22	+11.33	+430.29
	H_2O	−0.09	+30.31	−36.33
	O_2	−48.29	−36.8	−431.06 (−373.13)
$AuSn_{3.88}$	CO	−54.13	−34.78	+130.51
	H_2O	−136.42	−105.12	+158.79
	O_2	−210.23	−198.74	−276.04 (−369.19)

On the other hand, the introduction of defects on the surface leads to a negative value of ΔG for all the considered ambient gases. In particular, Figure 3a shows the optimized atomic structure of molecular oxygen physisorbed on the Sn vacancy in the surface layer of $AuSn_{3.88}$. It should be noted that, although CO adsorption is energetically favorable in $AuSn_{3.88}$ (ΔG = −34.79 kJ/mol), physisorption of molecular oxygen and water is largely preferential (ΔG values of −105.12 and −198.74 kJ/mol, respectively), so that the Sn-vacancy sites will be occupied before by O_2 and H_2O. Hence, $AuSn_4$-based electrodes can be considered as CO-tolerant.

Physisorption might be the first step toward decomposition of adsorbed molecules. To evaluate the possibility of this scenario, the differential enthalpy of decomposition ΔH_{dec} for water and molecular oxygen was calculated (values in Table 1, see Figure 3b for a visualization).

Water decomposition is energetically favorable only on the defect-free $AuSn_4$ surface (Table 1). One should consider that ΔH_{dec} for water was calculated considering the adsorption of water from air. However, in the case of water adsorption from liquid, the contribution from entropy should be smaller, since the energy of noncovalent interactions of water with $AuSn_4$ is smaller than the energy of hydrogen bonds with other water molecules. Therefore, spontaneous decomposition of water in liquid state could occur.

Since the decomposition energy of oxygen molecules is quite high (above 200 kJ/mol), we opted to simulate the oxidation of the entire surface (Figure 3c). The computational results (Table 1) clearly demonstrate that this process is highly energetically favorable for both of the substrates examined, with a value of approximately −370 kJ/mol. Therefore, similarly to other transition-metal stannides, such as $PtSn_4$[22] and $PdSn_4$,[10] the surface of $AuSn_4$ will be immediately oxidized. The chemical instability of the surface layer is caused by a combination of factors, including the presence of broken Sn−Sn interlayer bonds that occur during the formation of the Sn-terminated surface, as well as charge transfer between surface Sn and subsurface Au atoms (as shown in Figure 4a). Although the formation of the surface does not result in any additional peaks near the Fermi level (as indicated in Figure 4c), we propose that the second factor—the charge transfer—plays a more significant role in the chemical instability of the surface.

The formation of an oxidized layer induces both quantitative changes in the doping of the surface layer from the subsurface region and visible modifications in the electronic structure of the subsurface Au atomic layer (Figure 4d vs Figure 4e). The contribution of Au 5d-states to the topological features in the band structure near the Fermi level is significant (blue lines in Figure 2). Therefore, the oxidation of the Sn surface layer destroys the topological features in the Sn−Au−Sn trilayer. The changes in the electronic structure of the subsurface layer arise not only from charge redistribution, but also from the displacement of the Au atoms from their stoichiometric positions. In the bulk crystal layer, the Au atoms are precisely located between two Sn layers (as shown in Figure 1). However, the formation of the surface with the breakage of Sn−Sn interlayer bonds leads to a shift of the Au layer away from the surface (Figure 3a,b). This alteration in the symmetry of the subsurface layers results in a deviation of the electronic structure of the $AuSn_4$ slab from that of the bulk (Figure 3c,d vs Figure 2). Additionally, the oxidation of the entire Sn surface layer further displaces the Au layer into the bulk (Figure 3c). Therefore, changes in the electronic structure of subsurface layers are not only caused by the passivation of surface dangling bonds, but also by variations in the atomic structure of the subsurface layers.

The theoretical model was validated by experiments on the surface chemical reactivity of $AuSn_4$ by X-ray photoelectron spectroscopy (XPS), using a synchrotron light source to optimize the surface sensitivity and energy resolution. High-resolution XPS spectra of Au-4f, Sn-3d, and O-1s core levels for the as-cleaved $AuSn_4$ and the same surface modified by the exposure to 10^4 L (1L = 10^{-6} Torr s^{-1}) of O_2, H_2O, and CO are reported in Figure 5. Specifically, the Au-4f core level was recorded at a binding energy (BE) of 85.0 (J = 7/2) and 88.6 (J = 5/2) eV, congruently with other Au−Sn alloys.[26,27] The

https://doi.org/10.1021/acs.jpclett.3c00113
J. Phys. Chem. Lett. 2023, 14, 3069−3076

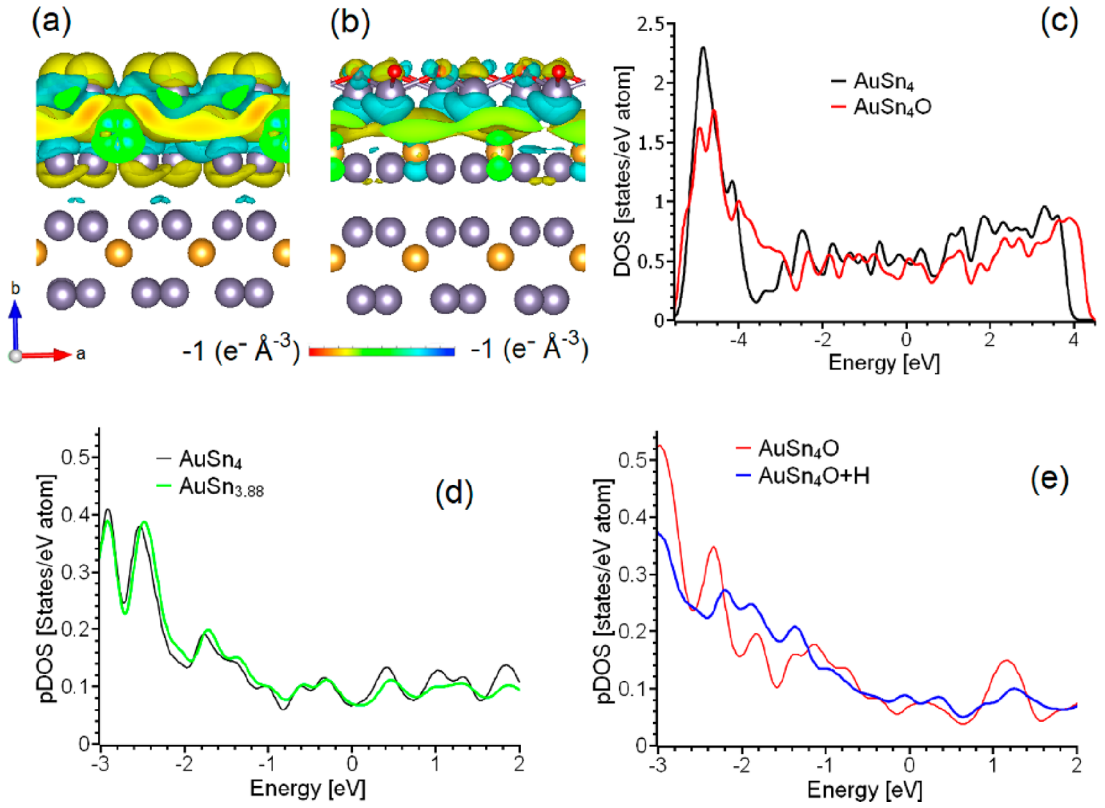

Figure 4. Changes of the charge density after formation of the interface between (a) surface Sn and (b) SnO_2 layers and the subsurface part of the $AuSn_4$ slab. Panel (c) reports the total densities of states for both structures shown on panels (a) and (b). Panels (d) and (e) report the partial densities of states (pDOS) of 5d orbitals of the Au atoms from subsurface layers for the cases of (d) $AuSn_4$ and $AuSn_{3.88}$ (in the latter case, the pDOS is shown for the Au atom closest to Sn vacancy), and for (e) $AuSn_4O$ and $AuSn_4O$+H (in the latter case, the pDOS is shown for the Au atom closest to adsorbed H).

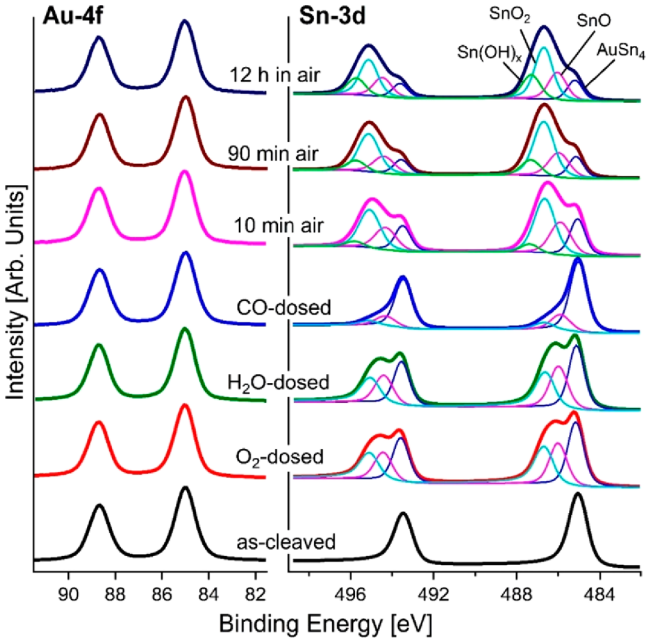

Figure 5. Core-level spectra of Au-4f and Sn-3d collected from as-cleaved $AuSn_4$ (black curve) and from the same surface exposed to O_2 (red curve), H_2O (green curve), and CO (blue curve). The $AuSn_4$ surface was also kept in air for different times: 10 min (pink curve), 90 min (brown curve), and 12 h (dark blue curve). The photon energy is 900 eV, and the spectra are normalized to the maximum.

spin−orbit split doublet was practically unchanged upon O_2, H_2O, and CO exposure. Correspondingly, the Sn-3d core level for as-cleaved $AuSn_4$ was recorded at a BE of 485.0 (J = 5/2) and 493.4 (J = 3/2) eV.[26] Upon O_2 exposure, two additional components arising from SnO and SnO_2 appeared in Sn-3d core levels, with the J = 5/2 components at 486.0 and 486.6 eV,[22,28] respectively, with intensities as high as 26% and 27% of the total spectral area. Similarly, H_2O dosage on $AuSn_4$ provided the same oxide components, with similar intensity.

On the other hand, with CO exposure a slight change in the spectra occurs with the formation of SnO (15% of the total spectral area) and SnO_2 (6.5% of the total spectral area). The analysis of O-1s spectra (Figure S1 in Supporting Information) confirms the formation of oxide species for the O_2- and H_2O-dosed samples.

The as-cleaved $AuSn_4$ was also directly exposed to air with the aim to assess its ambient stability. Au-4f and Sn-3d core-level spectra were measured as a function of exposure time to air to study the aging of $AuSn_4$, as reported in Figure 5 (see also Supporting Information, Figure S1 for O-1s). The intensity of the oxide-derived components in the Sn-3d core levels gradually increased from ∼64% (after 10 min in air) to ∼76% (after 12 h in air) of the total spectral area. Specifically, after 10 min in air the formation of SnO, SnO_2, and $Sn(OH)_x$[29−33] was evident in Sn-3d core levels, with a corresponding intensity of 23, 38, and 4% of the total spectral area, respectively. From 10 to 90 min in air, an enhancement of SnO_2 (43% of the total spectral area) and $Sn(OH)_x$ (11% of the total spectral area) components at the expense of SnO

https://doi.org/10.1021/acs.jpclett.3c00113
J. Phys. Chem. Lett. 2023, 14, 3069−3076

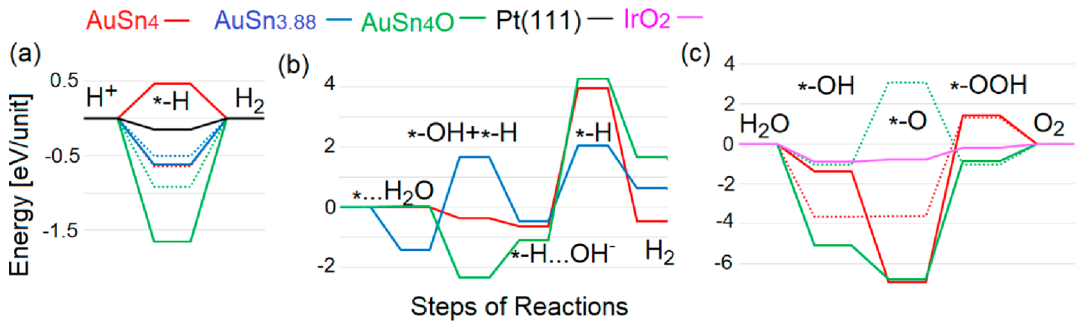

Figure 6. Free energy diagram for HER in (a) acidic and (b) alkali media and (c) OER in acidic media over $AuSn_4$-based substrates and reference compounds. The oxidized surface of $AuSn_4$ is denoted as $AuSn_4O$. Dotted lines correspond to the energies of the same processes over similar $PdSn_4$ substrates. The asterisk denotes the substrate, and "···" corresponds to physisorption.[35,36]

(20% of the total spectral area) was observed. After 12 h in air, hydroxylation of tin-oxide phases occurred, as indicated by the emergence of a $Sn(OH)_x$ component (18% of the total spectral area).

By means of quantitative XPS analysis,[34] we estimated the thickness of the oxide skin formed upon air exposure to be ∼2 nm, with passivation occurring in less than 15 min. The strong reactivity toward oxidation is also supported by considering that 10^4 L O_2 exposure in vacuum conditions already provided a oxide skin ∼1 nm thick.

To evaluate the effectiveness of $AuSn_4$ for catalysis, we assessed its effectiveness for the hydrogen evolution reaction (HER), oxygen evolution reaction (OER), and CO_2 reduction reaction (CO_2RR).

For HER in acid media (Figure 6a), the first step of the model is the Volmer reaction:

$$H^+ \rightarrow {}^*{-}H \tag{1}$$

i.e., the adsorption of hydrogen on the pristine and the oxidized (Figure 3d) surface. In the case of the pristine $AuSn_4$ surface, hydrogen adsorption should overcome an energy barrier of +0.46 eV. The presence of Sn vacancies or of a tin-oxide skin turn the Volmer step to an exothermic process with an energy of −0.62 and −1.66 eV, respectively (Figure 6a). The formation of the oxide layer corresponds to visible changes in the subsurface Au layer. The adsorption of hydrogen on the tin-oxide surface corresponds to the partial reduction of the surface layer, resulting in a visibly affected electronic structure of the subsurface Au layer (see Figure 4e). In contrast, the formation of a Sn vacancy does not have a visible effect on the electronic structure of the nearest Au atom (Figure 4d), and adsorption of hydrogen does not correspond to a reduction of the surface layer since the energy of the Heyrovsky step of the HER in acidic media (2) has the same magnitude of energy of the Volmer step, but with an opposite sign.

$$H^+ + {}^*{-}H \rightarrow H_2 \tag{2}$$

Thus, for both $AuSn_{3.88}$ and the oxidized $AuSn_4$, the Heyrovsky step requires overcoming a significant energy barrier. Thus, the Tafel step is the only viable alternative.

The Volmer step corresponds to the recombination of two hydrogen atoms adsorbed on the substrate:

$$2\,{}^*{-}H \rightarrow H_2 \tag{3}$$

The rate of this reaction is typically limited by the energy barrier for the migration of hydrogen atoms across the substrate. The Volmer step is often overlooked due to its high energy barrier. However, the unique atomic structure of oxidized $AuSn_4$ enables the migration of hydrogen atoms through the Sn−O layer with an energy cost of 0.19 eV. The breaking of the Sn−H bond (Figure 3d) is compensated by the interaction of hydrogen atoms with the electron cloud, which is distributed over the entire oxidized surface of $AuSn_4$. As a result, the oxidized surface of $AuSn_4$ is a favorable platform for HER in acidic media, due to the combination of the exothermic Volmer step and the low energy barrier for hydrogen atom migration over the surface.

Table 2. Calculated Gibbs Free Energies (in eV/mol) at Room Temperature of the Steps of CO_2 Reduction over Pristine and Oxidized $AuSn_4$ (Denoted as "ox-$AuSn_4$") Surface

step	reaction/substrate (*)	$AuSn_4$	ox-$AuSn_4$
1	H_2 + * → 2(*-H)	0.98	−3.30
2	CO_2 physisorption	0.83	0.35
3	CO_2 + 2(*-H) → *-H + *-COOH	−1.20	−1.77
4	*-H + *-COOH → *-H + *−OH + *-CO	0.38	1.26
5	*-H + *-OH + *-CO → *-CO + *-H_2O	-0.77	1.25
6	desorption of CO and H_2O	-0.24	−0.93

The first step of the CO_2RR involves the decomposition of molecular hydrogen on the surface of the catalyst. In the case of pristine $AuSn_4$, an energy barrier of 0.98 eV/H_2 exists, while for the oxidized $AuSn_4$ this step is exothermic (−3.30 eV/H_2), and, accordingly, molecular hydrogen will decompose. The next step of the reaction is the physisorption of carbon dioxide on the surface of the catalyst. For both considered surfaces, this step is endothermic, but the magnitude of the free energy required for adsorption on $AuSn_4$ is more than twice as large than over the oxidized surface (0.83 vs 0.35 eV/CO_2). Note that the energies required for physisorption of CO_2 on the oxidized surface are just moderate. The third step of the CO_2RR implicates the migration of the hydrogen atom adsorbed on the catalyst to carbon dioxide, with the subsequent transformation of the noncovalently adsorbed CO_2 to −COOH or carboxyl groups, covalently adsorbed on the substrate. Contrary to ceria, where this step is endothermic,[35,36] on $AuSn_4$ it is exothermic for both pristine and oxidized surfaces. Such a difference is connected to the presence of electronic states around the Fermi level (Figure 1e−f). These topological features in the electronic structure correspond to outstanding electrical transport properties and also to chemical activity of the surface. In the case of an

https://doi.org/10.1021/acs.jpclett.3c00113
J. Phys. Chem. Lett. 2023, 14, 3069−3076

oxidized surface, topological features in the electronic structure of subsurface layers also affect the chemical activity of the oxidized surface layer via doping. The fourth step of the reaction corresponds to the migration of the −OH group from the carboxyl group to the surface of the catalyst. This step is endothermic for both substrates, but, in the case of an oxidized surface, the energy cost of this step is larger, because all suitable sites for oxidation spots on the surface would be already occupied. The fifth, penultimate, step of the process corresponds to the diffusion of the second hydrogen atom adsorbed at the surface of the catalyst toward the hydroxyl (−OH) group with the formation of physisorbed water molecules at the surface. In the case of the nonoxidized $AuSn_4$ surface, the adsorption of hydrogen (first step of the reaction) and the hydroxyl group (fourth step of the reaction) is energetically unfavorable, resulting in the desorption of hydrogen from the surface and the favorable transformation of the hydroxyl group to water. In contrast, due to the strong adsorption of hydrogen atoms on the oxidized $AuSn_4$, this step of the reaction is energetically unfavorable. The final step of the reaction involves the desorption of the products (carbon monoxide and water molecules) from the catalyst surfaces, which is energetically favorable for both substrates. Thus, the results of our calculations indicate that carbon dioxide reduction over $AuSn_4$-based substrates involves alternating steps that are energetically favorable and unfavorable. For both substrates, the magnitudes of the values of free energies of exothermic steps overcome the energy costs of the endothermic steps. Note that the energy costs of the largest endothermic steps on both substrates (0.98 and 1.28 eV/mol) are of the same order (0.0−1.4 eV/mol) as those calculated for other prospective catalysts,[35,36] including platinum.[37] Thanks to the presence of topological features in the band structure that turn the rate-determining step of reaction to exothermic, both pure and oxidized $AuSn_4$ can be considered as promising catalysts for this reaction. Moreover, it is worth noting that the already-oxidized surface of $AuSn_4$ is expected to remain stable over time, unlike the nonoxidized surface, which is inherently unstable in air.

In conclusion, we have established a correlation between the exceptional catalytic activity of $AuSn_4$ in the HER and CO_2RR and the presence of topological electronic states. Contrary to previous reports, our model also considers the natural evolution of the catalyst's surface upon interaction with air and finds that surface oxidation is even beneficial for the HER. We demonstrate that the combination of the exothermic Volmer step and the low energy barrier for the migration of hydrogen atoms over the surface makes the oxidized surface of $AuSn_4$, a topological nodal-line semimetal, a suitable platform for HER in acidic media. Specifically, the theoretical model points out that the desorption of hydroxyl groups is the rate-determining step of HER in alkali conditions. For the oxidized $AuSn_4$ surface, the first steps of the HER in alkali media are exothermic with rather large magnitudes of the energies, which could partially compensate the energy cost of the desorption of the hydroxyl groups. Hence, oxidized $AuSn_4$ could be also considered as a catalyst of the HER in alkali media. Regarding CO_2RR, we find that $AuSn_4$ is a promising catalyst, due to the presence of topological electronic states. Specifically, the migration of the hydrogen atom adsorbed on rgw catalyst to carbon dioxide, with the subsequent conversion of the noncovalently adsorbed CO_2 to −COOH or carboxyl groups, is exothermic for both pristine and oxidized surfaces of $AuSn_4$. This is in contrast to other catalysts, including ceria, and is due to the presence of topological electronic states near the Fermi level, providing efficient electrical transport and subsequent superior chemical activity of the surface. In the case of the oxidized surface, the topological features in the electronic structure of subsurface layers also affect the chemical activity of the oxidized surface layer via doping.

Our results are significant in bringing quantum materials to fruition in catalysis, including the unforeseen role played by surface oxidation. Moreover, our findings can be applied to other materials with analogous physicochemical and structural properties.

Overall, our results shed light on the physicochemical mechanisms underlying catalytic reactions over the surfaces of quantum materials in the presence of an oxidizing ambient atmosphere. These findings also open new avenues for the design of high-performance catalysts based on topological nodal-line semimetals.

METHODS

Single-Crystal Growth and Cleavage. Single crystals of $AuSn_4$ were synthesized by the self-flux method. High-purity Au (99.99%) and Sn ingots (99.999%) were sealed in an evacuated quartz tube with a flat bottom. The mixed elements were heated for 6 h, dwelled for 10 h, quickly cooled to 350 °C in 5 h, and then slowly cooled at a rate of 1 °C/h to 250 °C. Subsequently, the excess Sn flux was removed by centrifugation and then etched in concentrated hydrochloric acid. The $AuSn_4$ crystals were cleaved in a ultrahigh vacuum by a postmethod with a natural cleavage plane coinciding with the (010) orientation.

ARPES Measurements. ARPES measurements on the $AuSn_4$ single crystals were performed at the APE-LE beamline of ELETTRA Synchrotron in Trieste, Italy, using a DA30 electron energy analyzer. The spectra presented here were acquired with 48 eV photon energy.

XPS Measurements. XPS experiments were performed at the High-Energy branch of the Advanced Photoelectric Experiments beamline (APE-HE) of the Elettra Synchrotron, Trieste, Italy. XPS spectra were acquired with an Omicron EA125 hemispherical electron energy analyzer, with the sample at room temperature and in normal emission conditions. The linearly polarized light was impinging on the sample forming an angle of 45 deg with respect to the normal to the surface. Under our experimental conditions, there is no beam-induced damage.

DFT Calculations. The atomic structure and energetics of various configurations was studied by DFT using the QUANTUM-ESPRESSO code[38] and the GGA−PBE,[39] taking into account van der Waals forces correction.[40] For all calculations, we used ultrasoft pseudopotentials.[41] The values of energy cutoffs were 25 and 400 Ry for the plane-wave expansion of the wave functions and the charge density, respectively. The possible influence of correlation effects on the electronic structure of $AuSn_4$ was checked by DFT+U calculations, which demonstrated their negligible influence on the band structure in the vicinity of the Fermi energy (see Figure S2).

The enthalpy of reaction is defined as difference in calculated total energies of products and reactant. Thus, negative enthalpy corresponds to exothermic reactions.

Physisorption enthalpies were calculated by the standard formula:

https://doi.org/10.1021/acs.jpclett.3c00113
J. Phys. Chem. Lett. 2023, 14, 3069−3076

$$\Delta H_{phys} = [E_{host+mol} - (E_{host} + E_{mol})]$$

where E_{host} is the total energy of pristine surface, and E_{mol} is the energy of the single molecules of selected species in empty box. In the case of water adsorption, we only considered the gaseous phase. Decomposition energy is defined as difference between the total energy of the system with the adsorbed molecule and the total energy of same system after decomposition of the same molecule on the surface. For the case of physisorption, we also evaluated differential Gibbs free energy by the formula:

$$\Delta G = \Delta H - T\Delta S$$

where T is the temperature and ΔS is the change of entropy of the adsorbed molecule, which was estimated considering the gas → liquid transition by the standard formula:

$$\Delta S = \Delta H_{vaporization}/T$$

where $\Delta H_{vaporization}$ is the measured enthalpy of vaporization.

■ ASSOCIATED CONTENT

Supporting Information

The Supporting Information is available free of charge at https://pubs.acs.org/doi/10.1021/acs.jpclett.3c00113.

O-1s core-level spectra; band structure calculated with DFT+U (PDF)

■ AUTHOR INFORMATION

Corresponding Author

Antonio Politano − *Department of Physical and Chemical Sciences, University of L'Aquila, 67100 L'Aquila (AQ), Italy;* orcid.org/0000-0002-4254-2102; Email: antonio.politano@univaq.it

Authors

Danil W. Boukhvalov − *College of Science, Institute of Materials Physics and Chemistry, Nanjing Forestry University, Nanjing 210037, P. R. China; Institute of Physics and Technology, Ural Federal University, 620002 Yekaterinburg, Russia;* orcid.org/0000-0002-2286-3443

Gianluca D'Olimpio − *Department of Physical and Chemical Sciences, University of L'Aquila, 67100 L'Aquila (AQ), Italy;* orcid.org/0000-0002-6367-3945

Federico Mazzola − *Consiglio Nazionale delle Ricerche (CNR), Istituto Officina dei Materiali (IOM), Laboratorio TASC, 34149 Trieste, Italy*

Chia-Nung Kuo − *Department of Physics, National Cheng Kung University, 70101 Tainan, Taiwan*

Sougata Mardanya − *Department of Physics, National Cheng Kung University, 70101 Tainan, Taiwan*

Jun Fujii − *Consiglio Nazionale delle Ricerche (CNR), Istituto Officina dei Materiali (IOM), Laboratorio TASC, 34149 Trieste, Italy*

Grazia Giuseppina Politano − *Department of Information Engineering, Infrastructures and Sustainable Energy (DIIES), University "Mediterranea" of Reggio Calabria, 89122 Reggio Calabria, Italy*

Chin Shan Lue − *Department of Physics, National Cheng Kung University, 70101 Tainan, Taiwan*

Amit Agarwal − *Department of Physics, Indian Institute of Technology Kanpur, Kanpur 208016, India*

Ivana Vobornik − *Consiglio Nazionale delle Ricerche (CNR), Istituto Officina dei Materiali (IOM), Laboratorio TASC, 34149 Trieste, Italy;* orcid.org/0000-0001-9957-3535

Piero Torelli − *Consiglio Nazionale delle Ricerche (CNR), Istituto Officina dei Materiali (IOM), Laboratorio TASC, 34149 Trieste, Italy*

Complete contact information is available at: https://pubs.acs.org/10.1021/acs.jpclett.3c00113

Author Contributions

#D.W.B. and G.D. contributed equally.

Notes

The authors declare no competing financial interest.

■ REFERENCES

(1) Kang, L.; Cao, Z. Y.; Wang, B. Pressure-Induced Electronic Topological Transition and Superconductivity in Topological Insulator $Bi_2Te_{2.1}Se_{0.9}$. *J. Phys. Chem. Lett.* **2022**, *13* (49), 11521−11527.

(2) Kirby, R. J.; Scholes, G. D.; Schoop, L. M. Square-Net Topological Semimetals: How Spectroscopy Furthers Understanding and Control. *J. Phys. Chem. Lett.* **2022**, *13* (3), 838−850.

(3) Kong, X.-P.; Jiang, T.; Gao, J.; Shi, X.; Shao, J.; Yuan, Y.; Qiu, H.-J.; Zhao, W. Development of a Ni-Doped VAl_3 Topological Semimetal with a Significantly Enhanced HER Catalytic Performance. *J. Phys. Chem. Lett.* **2021**, *12* (15), 3740−3748.

(4) Li, Y.; Zhang, Y. F.; Deng, J.; Dong, W. H.; Sun, J. T.; Pan, J.; Du, S. Rational Design of Heteroanionic Two-Dimensional Materials with Emerging Topological, Magnetic, and Dielectric Properties. *J. Phys. Chem. Lett.* **2022**, *13* (16), 3594−3601.

(5) Borca, B.; Castenmiller, C.; Tsvetanova, M.; Sotthewes, K.; Rudenko, A. N.; Zandvliet, H. J. W. Image potential states of germanene. *2D Mater.* **2020**, *7* (3), 035021.

(6) Sahni, B.; Vikram; Kangsabanik, J.; Alam, A. Reliable Prediction of New Quantum Materials for Topological and Renewable-Energy Applications: A High-Throughput Screening. *J. Phys. Chem. Lett.* **2020**, *11* (15), 6364−6372.

(7) Xu, H.; Zhou, J.; Wang, H.; Li, J. Giant photonic response of mexican-hat topological semiconductors for mid-infrared to terahertz applications. *J. Phys. Chem. Lett.* **2020**, *11* (15), 6119−6126.

(8) Yan, M.; Lu, J.; Li, F.; Deng, W.; Huang, X.; Ma, J.; Liu, Z. On-chip valley topological materials for elastic wave manipulation. *Nat. Mater.* **2018**, *17* (11), 993−998.

(9) Rajamathi, C. R.; Gupta, U.; Kumar, N.; Yang, H.; Sun, Y.; Süß, V.; Shekhar, C.; Schmidt, M.; Blumtritt, H.; Werner, P.; Yan, B.; Parkin, S.; Felser, C.; Rao, C. N. R. Weyl Semimetals as Hydrogen Evolution Catalysts. *Adv. Mater.* **2017**, *29* (19), 1606202.

(10) Boukhvalov, D. W.; Kuo, C.-N.; Nappini, S.; Marchionni, A.; D'Olimpio, G.; Filippi, J.; Mauri, S.; Torelli, P.; Lue, C. S.; Vizza, F.; Politano, A. Efficient Electrochemical Water Splitting with $PdSn_4$ Dirac Nodal Arc Semimetal. *ACS Catal.* **2021**, *11*, 7311−7318.

(11) Qu, Q.; Liu, B.; Liang, J.; Li, H.; Wang, J.; Pan, D.; Sou, I. K. Expediting Hydrogen Evolution through Topological Surface States on Bi_2Te_3. *ACS Catal.* **2020**, *10* (4), 2656−2666.

(12) Shen, D.; Kuo, C. N.; Yang, T. W.; Chen, I. N.; Lue, C. S.; Wang, L. M. Two-dimensional superconductivity and magnetotransport from topological surface states in $AuSn_4$ semimetal. *Communications Materials* **2020**, *1* (1), 56.

(13) Hu, J.; Xu, S.-Y.; Ni, N.; Mao, Z. Transport of Topological Semimetals. *Annu. Rev. Mater. Res.* **2019**, *49* (1), 207−252.

(14) Yang, Q.; Li, G.; Manna, K.; Fan, F.; Felser, C.; Sun, Y. Topological Engineering of Pt-Group-Metal-Based Chiral Crystals toward High-Efficiency Hydrogen Evolution Catalysts. *Adv. Mater.* **2020**, *32* (14), 1908518.

(15) Rajamathi, C. R.; Gupta, U.; Kumar, N.; Yang, H.; Sun, Y.; Suss, V.; Shekhar, C.; Schmidt, M.; Blumtritt, H.; Werner, P.; Yan, B.;

Parkin, S.; Felser, C.; Rao, C. N. R. Weyl Semimetals as Hydrogen Evolution Catalysts. *Adv. Mater.* **2017**, *29* (19), 1606202.
(16) Mun, E.; Ko, H.; Miller, G. J.; Samolyuk, G. D.; Bud'Ko, S. L.; Canfield, P. C. Magnetic field effects on transport properties of $PtSn_4$. *Phys. Rev. B* **2012**, *85* (3), 035135.
(17) Xu, C. Q.; Zhou, W.; Sankar, R.; Xing, X. Z.; Shi, Z. X.; Han, Z. D.; Qian, B.; Wang, J. H.; Zhu, Z.; Zhang, J. L.; Bangura, A. F.; Hussey, N. E.; Xu, X. Enhanced electron correlations in the binary stannide $PdSn_4$: A homologue of the Dirac nodal arc semimetal $PtSn_4$. *Phys. Rev. Mater.* **2017**, *1* (6), 064201.
(18) Jo, N. H.; Wu, Y.; Wang, L.-L.; Orth, P. P.; Downing, S. S.; Manni, S.; Mou, D.; Johnson, D. D.; Kaminski, A.; Bud'ko, S. L.; Canfield, P. C. Extremely large magnetoresistance and Kohler's rule in $PdSn_4$: A complete study of thermodynamic, transport, and band-structure properties. *Phys. Rev. B* **2017**, *96* (16), 165145.
(19) Kubiak, R.; Wolcyrz, M. Refinement of the crystal structures of $AuSn_4$ and $PdSn_4$. *J. Less Common Met.* **1984**, *97*, 265−269.
(20) Kubiak, R.; Wołcyrz, M. X-ray investigations of crystallization and thermal expansion of $AuSn_4$, $PdSn_4$ and $PtSn_4$. *J. Less Common Met.* **1985**, *109* (2), 339−344.
(21) Brun, C.; Cren, T.; Roditchev, D. Review of 2D superconductivity: the ultimate case of epitaxial monolayers. *Supercond. Sci. Technol.* **2017**, *30* (1), 013003.
(22) D'Olimpio, G.; Boukhvalov, D. W.; Fujii, J.; Torelli, P.; Marchionni, A.; Filippi, J.; Kuo, C.-N.; Edla, R.; Ottaviano, L.; Lue, C. S.; Vizza, F.; Nappini, S.; Politano, A. Catalytic activity of $PtSn_4$: insights from surface-science spectroscopies. *Appl. Surf. Sci.* **2020**, *514*, 145925.
(23) Boukhvalov, D. W.; Edla, R.; Cupolillo, A.; Fabio, V.; Sankar, R.; Zhu, Y.; Mao, Z.; Hu, J.; Torelli, P.; Chiarello, G.; Ottaviano, L.; Politano, A. Surface Instability and Chemical Reactivity of ZrSiS and ZrSiSe Nodal-Line Semimetals. *Adv. Funct. Mater.* **2019**, *29* (18), 1900438.
(24) Li, G.; Fu, C.; Shi, W.; Jiao, L.; Wu, J.; Yang, Q.; Saha, R.; Kamminga, M. E.; Srivastava, A. K.; Liu, E.; Yazdani, A. N.; Kumar, N.; Zhang, J.; Blake, G. R.; Liu, X.; Fahlman, M.; Wirth, S.; Auffermann, G.; Gooth, J.; Parkin, S.; Madhavan, V.; Feng, X.; Sun, Y.; Felser, C. Dirac Nodal Arc Semimetal $PtSn_4$: An Ideal Platform for Understanding Surface Properties and Catalysis for Hydrogen Evolution. *Angew. Chem.* **2019**, *58* (37), 13107−13112.
(25) Lamuta, C.; Campi, D.; Pagnotta, L.; Dasadia, A.; Cupolillo, A.; Politano, A. Determination of the mechanical properties of SnSe, a novel layered semiconductor. *J. Phys. Chem. Solids* **2018**, *116*, 306−312.
(26) Renault, O.; Garnier, A.; Morin, J.; Gambacorti, N.; Bertin, F. High-resolution XPS spectromicroscopy study of micro-patterned gold−tin surfaces. *Appl. Surf. Sci.* **2012**, *258* (24), 10077−10083.
(27) Sadhukhan, P.; Barman, S.; Roy, T.; Singh, V. K.; Sarkar, S.; Chakrabarti, A.; Barman, S. R. Electronic structure of Au-Sn compounds grown on Au(111). *Phys. Rev. B* **2019**, *100* (23), 235404.
(28) Kwoka, M.; Ottaviano, L.; Passacantando, M.; Santucci, S.; Czempik, G.; Szuber, J. XPS study of the surface chemistry of L-CVD SnO_2 thin films after oxidation. *Thin Solid Films* **2005**, *490* (1), 36−42.
(29) Boukhvalov, D. W.; Marchionni, A.; Filippi, J.; Kuo, C.-N.; Fujii, J.; Edla, R.; Nappini, S.; D'Olimpio, G.; Ottaviano, L.; Lue, C. S.; Torelli, P.; Vizza, F.; Politano, A. Efficient hydrogen evolution reaction with platinum stannide $PtSn_4$ via surface oxidation. *J. Mater. Chem. A* **2020**, *8* (5), 2349−2355.
(30) Jugnet, Y.; Loffreda, D.; Dupont, C.; Delbecq, F.; Ehret, E.; Cadete Santos Aires, F. J.; Mun, B. S.; Aksoy Akgul, F.; Liu, Z. Promoter Effect of Early Stage Grown Surface Oxides: A Near-Ambient-Pressure XPS Study of CO Oxidation on PtSn Bimetallics. *J. Phys. Chem. Lett.* **2012**, *3* (24), 3707−14.
(31) Du, W.; Mackenzie, K. E.; Milano, D. F.; Deskins, N. A.; Su, D.; Teng, X. Palladium−tin alloyed catalysts for the ethanol oxidation reaction in an alkaline medium. *ACS Catal.* **2012**, *2* (2), 287−297.
(32) Wu, P.; Huang, Y.; Kang, L.; Wu, M.; Wang, Y. Multisource Synergistic Electrocatalytic Oxidation Effect of Strongly Coupled PdM (M = Sn, Pb)/N-doped Graphene Nanocomposite on Small Organic Molecules. *Sci. Rep.* **2015**, *5* (1), 14173.
(33) Jadhav, H.; Suryawanshi, S.; More, M. A.; Sinha, S. Pulsed laser deposition of tin oxide thin films for field emission studies. *Appl. Surf. Sci.* **2017**, *419*, 764−769.
(34) Cimino, A.; Gazzoli, D.; Valigi, M. XPS quantitative analysis and models of supported oxide catalysts. *J. Electron Spectrosc. Relat. Phenom.* **1999**, *104* (1−3), 1−29.
(35) Liu, X.; Xiao, J.; Peng, H.; Hong, X.; Chan, K.; Nørskov, J. K. Understanding trends in electrochemical carbon dioxide reduction rates. *Nat. Commun.* **2017**, *8* (1), 15438.
(36) Kildgaard, J. V.; Hansen, H. A.; Vegge, T. DFT+U study of CO_2 reduction and CO oxidation on a reconstructed CeO_{2-x}(110) facet. *Materials Today Advances* **2020**, *8*, 100111.
(37) Niu, J.; Du, X.; Ran, J.; Wang, R. Dry (CO_2) reforming of methane over Pt catalysts studied by DFT and kinetic modeling. *Appl. Surf. Sci.* **2016**, *376*, 79−90.
(38) Giannozzi, P.; Baroni, S.; Bonini, N.; Calandra, M.; Car, R.; Cavazzoni, C.; Ceresoli, D.; Chiarotti, G. L; Cococcioni, M.; Dabo, I.; Dal Corso, A.; de Gironcoli, S.; Fabris, S.; Fratesi, G.; Gebauer, R.; Gerstmann, U.; Gougoussis, C.; Kokalj, A.; Lazzeri, M.; Martin-Samos, L.; Marzari, N.; Mauri, F.; Mazzarello, R.; Paolini, S.; Pasquarello, A.; Paulatto, L.; Sbraccia, C.; Scandolo, S.; Sclauzero, G.; Seitsonen, A. P; Smogunov, A.; Umari, P.; Wentzcovitch, R. M QUANTUM ESPRESSO: a modular and open-source software project for quantum simulations of materials. *J. Phys.: Condens. Matter* **2009**, *21* (39), 395502.
(39) Perdew, J. P.; Burke, K.; Ernzerhof, M. Generalized Gradient Approximation Made Simple. *Phys. Rev. Lett.* **1996**, *77* (18), 3865−3868.
(40) Barone, V.; Casarin, M.; Forrer, D.; Pavone, M.; Sambi, M.; Vittadini, A. Role and effective treatment of dispersive forces in materials: Polyethylene and graphite crystals as test cases. *J. Comput. Chem.* **2009**, *30* (6), 934−939.
(41) Vanderbilt, D. Soft self-consistent pseudopotentials in a generalized eigenvalue formalism. *Phys. Rev. B* **1990**, *41* (11), 7892−7895.

https://doi.org/10.1021/acs.jpclett.3c00113
J. Phys. Chem. Lett. 2023, 14, 3069−3076